Nanoscale

PAPER

CrossMark
← click for updates

Self-assembled 3D hierarchical sheaf-like Nb$_3$O$_7$(OH) nanostructures with enhanced photocatalytic activity†

Pei Hu,[a] Dongfang Hou,[a,b] Yanwei Wen,[a] Bin Shan,[a] Chaoji Chen,[a] Yunhui Huang*[a] and Xianluo Hu*[a]

Novel three-dimensional (3D) hierarchical Nb$_3$O$_7$(OH) nanostructures with a sheaf-like nanoarchitecture were fabricated for the first time by a hydrothermal process. Interestingly, the nanosheafs are composed of nanorods with an average diameter of about 25 nm. The as-prepared 3D hierarchical nanostructures possess a high surface area of 77 m^2 g^{-1} with pore diameters of *ca.* 4.2–12.5 nm. A possible growth mechanism based on the combined Ostwald ripening and self-assembly process was proposed. It is found that both the valence-band top and the conduction-band bottom consist of O 2p and Nb 4d orbitals. Importantly, the 3D hierarchical Nb$_3$O$_7$(OH) nanostructures exhibit enhanced photocatalytic activity for the degradation of Rhodamine B (RhB) under UV-visible light, which is attributed to the unusual hierarchical structure, high surface area, and hybridization of energy bands.

Introduction

It is generally believed that the physical and chemical properties of nanomaterials depend not only on their chemical composition, but also on their structures, including phase, size, size distribution, morphology, and dimensionality.[1–6] Recently, three-dimensional (3D) complex architectures assembled with nanorods, nanobelts, or nanowires as one-dimensional (1D) nanoscale building blocks have attracted increasing attention because of their potential applications in catalytic, electronic, magnetic, optoelectronic, and biomedical fields. In this regard, a remarkable progress has been made for the synthesis of complex inorganic materials with controlled architectures, sizes, morphologies and patterns since these parameters represent key elements that determine their electrical and catalytic properties. Among various synthetic methods, the hard or soft templates are usually used to control their oriented growth, which not only introduces heterogeneous impurities, but also increases production costs. Therefore, the development of facile, template-free and self-assembly routes

for the formation of 3D hierarchical nanostructures is of great interest.[7–10] However, it is still highly challenging but desirable to design novel 3D nanomaterials with ideal, controllable and stable morphologies, sizes and structures.

Recently, great attention has been paid to the development of semiconductor photocatalysts with high activities because of wide applications such as the decomposition of organic contaminants, the production of clean hydrogen energy by splitting water, and CO$_2$ conversion to hydrocarbon fuel.[11–14] It is also reported that semiconductor nanostructures exhibit shape-dependent optical properties.[15,16] It is well-known that the photocatalytic activity is highly dependent on the phase, morphology, size, and surface area of photocatalysts.[17] Therefore, a nanoarchitecture with controllable morphology and large surface area is particularly crucial to semiconductor photocatalysts.

Niobium-containing compounds have been widely investigated for photocatalysts, lithium-ion batteries, and solar cells owing to their favourable properties such as non-toxicity, chemical inertness, and high stability under light irradiation. For example, Nb$_2$O$_5$ as an n-type transition metal-oxide semiconductor has attracted a great deal of interest in gas sensing, catalysis, and energy storage.[18–20] Various synthesis methods have been employed to fabricate Nb$_2$O$_5$ nanostructures with different morphologies, such as nanoparticles, nanotubes, nanobelts and nanoforests, which have exhibited promising applications in different fields.[21] However, only a few studies on other analogies of niobium-containing materials have been reported to date. For instance, several reports have indicated that Nb$_3$O$_7$(OH) is a class of important niobium-containing

*a*State Key Laboratory of Materials Processing and Die & Mould Technology, School of Materials Science and Engineering, Huazhong University of Science and Technology, Wuhan 430074, China. E-mail: huxl@mail.hust.edu.cn, huangyh@mail.hust.edu.cn
*b*College of Material and Chemical Engineering, Three Gorges University, Yichang 443002, China

materials with high crystallinity. It can be readily transformed into Nb_2O_5 with different crystal phases through thermal conversion. In 1978, Kodama *et al.*[22] reported the synthesis of $Nb_3O_7(OH)$ nanorods by hydrothermally treating niobic acid or triniobium chloride heptaoxide with sulfuric acid, but no detailed electronic structure information and practical applications were given in their work. Very recently, Zhao *et al.*[23] fabricated an $Nb_3O_7(OH)$ single crystal nanorod film on an F-doped SnO_2 (FTO) transparent conductive glass for solar cells and the crystal structure of $Nb_3O_7(OH)$ has been precisely identified based on the experimental data and theoretical calculations. Nevertheless, as far as we know, there is no report on a controllable assembly of $Nb_3O_7(OH)$ nanorods into 3D superstructures.

Herein, we successfully synthesized 3D high-crystalline hierarchical $Nb_3O_7(OH)$ nanostructures with a representative morphology of six-direction sheaf-like nanoarchitectures *via* a facile hydrothermal self-assembly route for the first time. The individual sheaf is composed of uniform single-crystal nanorods with an average diameter of 25 nm and an average length of 1 μm. The formation mechanism of hierarchical $Nb_3O_7(OH)$ nanostructures is also proposed. The photocatalytic activities of the resulting products for the degradation of RhB were evaluated under UV-visible light. Moreover, the electronic structure including the bandgap as well as the constitution of the valence and the conduction bands was discussed.

Experimental

Materials synthesis

The following chemicals were used as received without further purification. Niobium(v) chloride ($NbCl_5$, 99.9%) and hydrochloric acid (HCl, 37%) were purchased from Aladdin and Sinopharm Chemical Regent Co., Ltd, respectively. In a typical procedure, 0.324 g of niobium(v) chloride ($NbCl_5$) was dissolved in 20 mL of 6 M hydrochloric acid. After stirring for 1 min, the mixed solution involving $NbCl_5$ and HCl was transferred into a Teflon-lined stainless steel autoclave with a volume of 75 mL. After treating the mixed solution at 210 °C for 24 h, the autoclave was cooled to room temperature. The product was collected, washed with deionized water and absolute ethanol, and dried under vacuum at 80 °C for 12 h. Finally, powdered $Nb_3O_7(OH)$ was obtained for further characterization.

For comparison, $Nb_3O_7(OH)$ with different morphologies was also prepared *via* a solvothermal method by varying the amounts of $NbCl_5$ over a range from 0.21 to 0.43 g. Nb_2O_5 was prepared by the optimized thermal treatment of 3D hierarchical $Nb_3O_7(OH)$ nanostructures at 450 °C for 2 h.

Material characterization

X-ray diffraction (XRD) analysis was performed by using a Rigaku D/MAX-RB diffractometer using filtered Cu Kα radiation. The full diffraction patterns of the products were taken in the 2θ range from 10° to 80° at a step model with a step size of 0.02°. The average grain size of the samples was estimated using the Scherrer formula. The morphology of the samples was characterized using field-emission scanning electron microscopy (FE-SEM, SIRION200, Holland; accelerating voltage: 10 kV). Transmission electron microscopy (TEM) images and the corresponding selected-area electron diffraction (SAED) were recorded by using a JEOL JEM-2010F microscope. X-Ray photoelectron spectroscopy (XPS) measurements were carried out on a VG MultiLab 2000 system with a monochromatic Al Kα X-ray source (ThermoVG Scientific). UV-vis diffuse reflectance spectra were recorded on a SHIMADZU UV-2550 spectrophotometer with an integrating sphere, and $BaSO_4$ was used as the reference. The Brunauer–Emmett–Teller (BET) surface area was determined by nitrogen sorption using a Micromeritics ASAP 2020 analyzer.

Theoretical calculations

The electronic structure calculations were performed by using the density-functional theory as implemented in the plane-wave-basis-set VASP code.[24,25] The energy cutoff for the plane-wave expansion was set to be 280 eV. The Perdew–Burke–Ernzerhof (PBE) of the generalized gradient approximation (GGA) was used as the exchange-correlation function.[26] The hybrid functional Heyd–Scuseria–Ernzerhof (HSE) method was also used to underestimate the bandgaps of the semiconductors and insulators.[27] The Brillouin-zone was sampled according to the Monkhorst–Pack scheme using a Γ centered k-point mesh of 5 × 5×5 for a conventional unit cell of $Nb_3O_7(OH)$.

Activity evaluation

The photochemical reactor was a self-made cylindrical glass vessel with a water-cooling jacket. The photocatalytic activities of the as-obtained samples were characterized by the degradation of RhB under irradiation of a 500 W Xe lamp at ambient temperature. The irradiation distance between the lamp and the sample was 12 cm. In a typical procedure, the RhB solution (100 mL, 10^{-5} mol L^{-1}) containing 0.100 g of $Nb_3O_7(OH)$ was put in a homemade reactor. The suspension was stirred for 30 min in the dark to reach an adsorption–desorption equilibrium of RhB molecules on the surface of the catalysts and was then exposed to a 500 W Xe lamp. At a given time interval, 3 mL of the reaction solution was taken out of the suspension and immediately centrifuged at 12 000 rpm for 4 min. The supernatants were analyzed by UV/Vis spectroscopy (Shimadzu UV2550). The reaction was performed under constant magnetic stirring under ambient conditions.

Results and discussion

HCl is used to provide an apt acidic reaction environment and control the hydrolysis rate of $NbCl_5$ in the hydrothermal self-assembly process. Fig. 1a and b show the typical FESEM images of the products. As shown in Fig. 1a, the as-prepared $Nb_3O_7(OH)$ hierarchical nanostructure is entirely composed of uniform six-direction straw-like sheaves. Each individual sheaf has a diameter of about 1–1.5 μm with an average length of
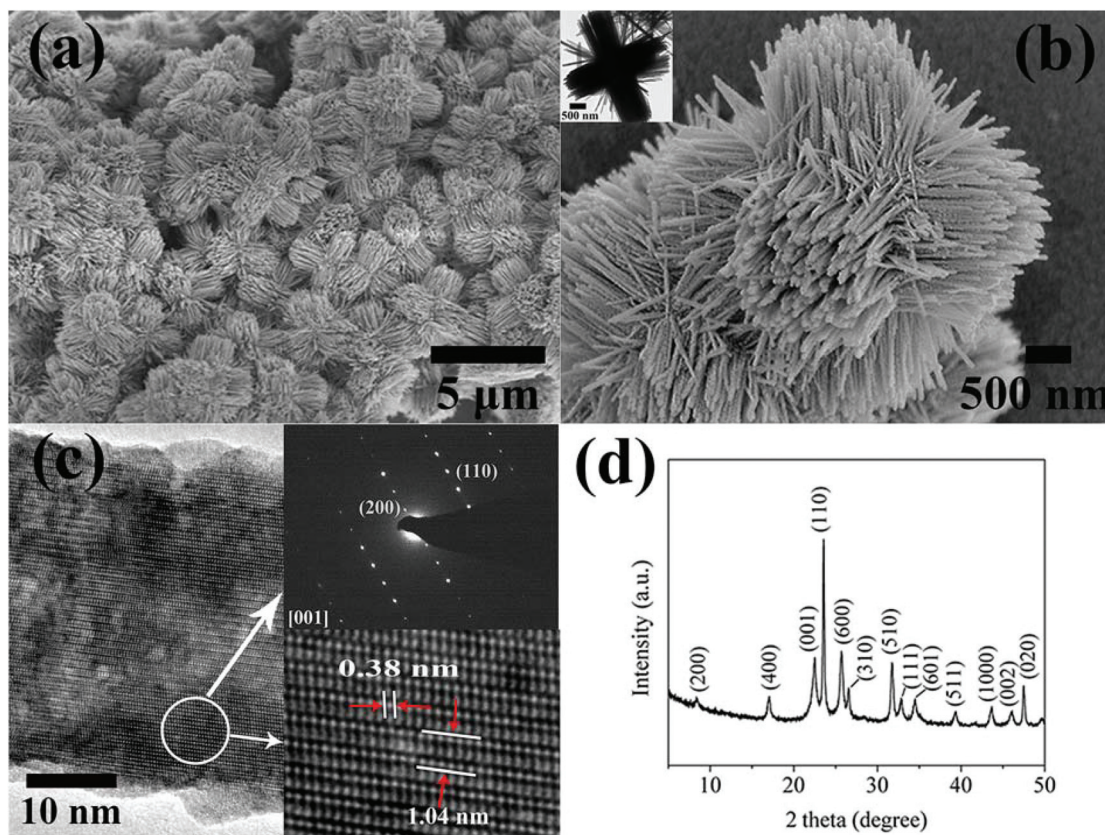
Fig. 1 (a,b) SEM image of the as-synthesized $Nb_3O_7(OH)$ hierarchical nanostructures. Inset: low-magnification TEM image. (c) TEM image of an individual $Nb_3O_7(OH)$ nanorod (top inset: SAED pattern; bottom inset: HRTEM image). (d) XRD pattern of the $Nb_3O_7(OH)$ product obtained at 210 °C for 24 h.

about 1–1.5 μm (Fig. 1b). Interestingly, the symmetric straw-sheaves are assembled from well-aligned nanorods with an average diameter of 25 nm and radially projecting out in six directions. The low-magnification TEM image in the inset of Fig. 1b exhibits the relative vertical direction of the six-direction nanorod bounds. Fig. 1c shows the representative TEM images of an individual $Nb_3O_7(OH)$ nanorod. The HRTEM image (bottom inset in Fig. 1c) and SAED (top inset in Fig. 1c) pattern display a single-crystalline nature of the nanorod with a preferential growth direction of [010].[23] The periodic fringe spacing of 0.38 nm and 1.04 nm could be assigned to the interplanar distances of (110) and (200) planes of orthorhombic $Nb_3O_7(OH)$, respectively.[22] Fig. 1d shows the XRD pattern of the as-synthesized sample obtained at 210 °C for 24 h. All the diffraction peaks could be readily indexed to the orthorhombic $Nb_3O_7(OH)$ structure (JCPDS no. 31-0928) with lattice parameters of a = 20.74 Å, b = 3.823 Å and c = 3.936 Å. No other impurities could be observed in the XRD pattern. The most stable structure (Fig. S1, see ESI†) was found to be configured after the lattice constants and atomic coordinates were fully optimized. Furthermore, a monoclinic Nb_2O_5 replica with the same morphology was obtained through thermal treatment of the resulting hierarchical $Nb_3O_7(OH)$ nanostructures (Fig. S2, see ESI†).

The influence of reactant concentration on the self-assembly process of the product was investigated. By varying the amount of $NbCl_5$ urchin-like structures (Fig. S3a, see ESI†) and irregular powders (Fig. S3b, see ESI†) could be obtained. In addition, time-dependent experiments were carried out.
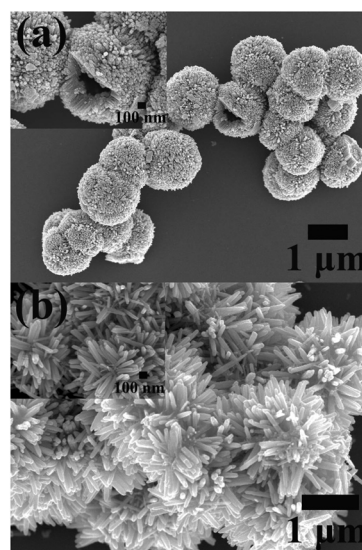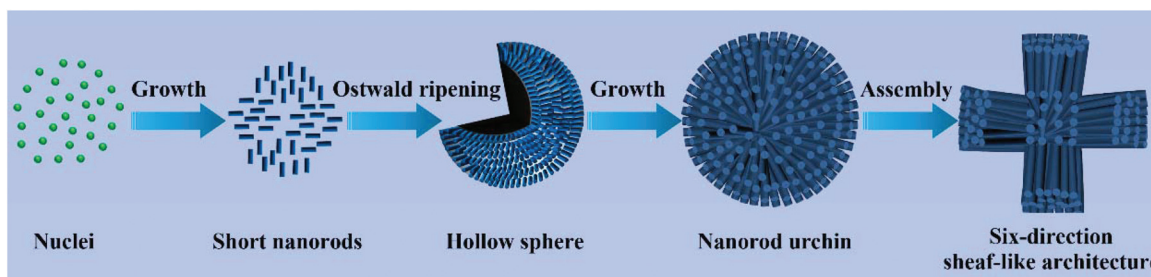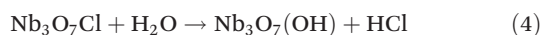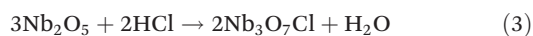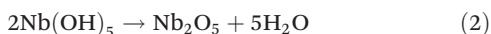

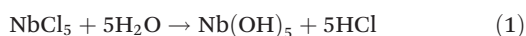**Fig. 2** SEM images of the as-prepared $Nb_3O_7(OH)$ hierarchical nanostructures prepared at 210 °C for different reaction times: (a) 3 h and (b) 12 h.

Scheme 1 Schematic illustration of the proposed formation process of 3D $Nb_3O_7(OH)$ hierarchical nanostructures.

Hollow microspheres composed of small nanorods with an average diameter of ~25 nm and an average length of 200 nm were obtained at early stages (3 h, 210 °C, Fig. 2a). When the reaction time was prolonged to 12 h, the nanorods which were aggregated into small bundles became longer with an average length of 1 μm and the microspheres disappeared (Fig. 2b). Further increasing the reaction time to 24 h generated sheaf-like structures with six-direction straw-sheaves assembled from well-aligned nanorods (Fig. 1b). The possible formation process for the six-direction sheaf-like hierarchical structure is shown in Scheme 1. The initially formed short nanorods of $Nb_3O_7(OH)$ tend to aggregate to reduce their surface energy after the nucleation process. The formation of the novel six-direction sheaf-like hierarchical structure may be attributed to the synergistic effects of Ostwald ripening and self-assembly processes. Based on the above results, the possible process for the formation of $Nb_3O_7(OH)$ hierarchical nanostructures could be explained as follows. Firstly, $NbCl_5$ slowly hydrolyzes into $Nb(OH)_5$, and then $Nb(OH)_5$ turns into Nb_2O_5 by the condensation reaction (eqn (1) and (2)). The formation kinetics of Nb_2O_5 is primarily determined by the reaction rate of eqn (1). Nb_2O_5 can further instantly react with HCl to form Nb_3O_7Cl at a certain temperature according to eqn (3). Finally, $Nb_3O_7(OH)$ nuclei are formed by hydrolyzing Nb_3O_7Cl at a high temperature and pressure (eqn (4)) and they grow into nanorods. As no surfactants or templates are involved, these initially formed 1D short nanorods are quickly built and spontaneously aggregate into hollow spheres to reduce their surface energy through the process known as Ostwald ripening. With the continuous growth of the nanorod along the [010] direction, the hollow spheres disappear, resulting in the formation of the urchin-like structure. After further growth, the bundles become larger and radically project out in six directions to be in a more stable state through self-assembly.

$$NbCl_5 + 5H_2O \rightarrow Nb(OH)_5 + 5HCl \qquad (1)$$

$$2Nb(OH)_5 \rightarrow Nb_2O_5 + 5H_2O \qquad (2)$$

$$3Nb_2O_5 + 2HCl \rightarrow 2Nb_3O_7Cl + H_2O \qquad (3)$$

$$Nb_3O_7Cl + H_2O \rightarrow Nb_3O_7(OH) + HCl \qquad (4)$$

Important information on the surface chemical state and the composition of the final products can be further provided by XPS studies. The survey XPS spectrum indicates the exist-

ence of Nb and O in the product (Fig. S4a, see ESI†). The element of H could not be detected directly by XPS. Two peaks at 209.7 and 206.9 eV are attributed to Nb $3d_{3/2}$ and Nb $3d_{5/2}$, respectively (Fig. S4b, see ESI†). The deconvolution of the O 1s spectrum indicates two contributions of lattice oxygen (O^{2-}) bound to niobium at a lower binding energy of 530.0 eV, and chemisorbed oxygen-containing species at a higher bonding energy of 531.9 eV, respectively, which confirm the presence of OH groups (Fig. S4c, see ESI†).[20,22,28,29]

The nitrogen adsorption–desorption isotherms of the 3D hierarchical $Nb_3O_7(OH)$ product and the corresponding pore size distribution curves are shown in Fig. 3. The specific surface area calculated by the multipoint Brunauer–Emmett–Teller (BET) method is 77 m^2 g^{-1}. The $Nb_3O_7(OH)$ hierarchical nanostructures display a type IV isotherm with a type H3 hysteresis loop (at $P/P_0 \geq 0.8$), implying the presence of mesopores.[30,31] The corresponding pore-size distribution also indicates the presence of mesopores (inset in Fig. 3). The pore size distribution shows a relative wide range with massive mesopores and macropores. Typical pores with diameters of *ca.* 4.2–12.5 nm may be generated during the crystal growth process, whereas larger pores can be attributed to the space between the well-aligned $Nb_3O_7(OH)$ nanorods.[30]
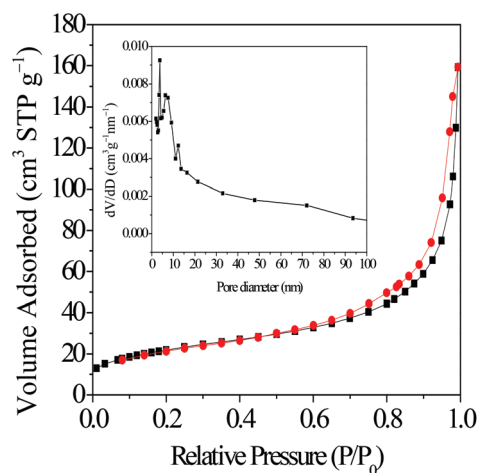

Fig. 3 Typical nitrogen adsorption–desorption isotherm of the 3D $Nb_3O_7(OH)$ hierarchical architecture. Inset: the corresponding pore-size distribution.
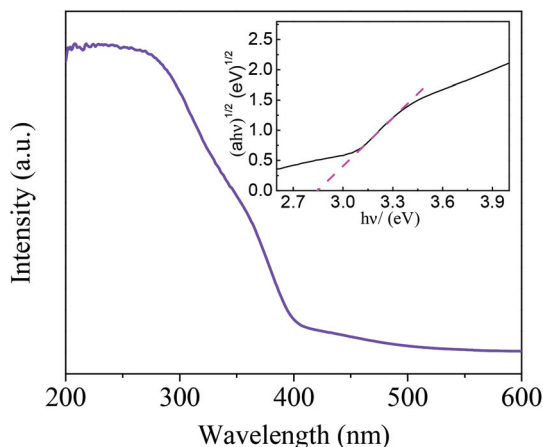
Fig. 4 UV-vis absorption spectrum of the as-synthesized $Nb_3O_7(OH)$ hierarchical nanostructures. The inset shows the relationship between $(\alpha h\nu)^2$ and photon energy.

Fig. 5 Band structures and partial density of states of the as-prepared $Nb_3O_7(OH)$.

The UV-vis diffuse reflectance spectrum of the synthesized six-way sheaf-like $Nb_3O_7(OH)$ is shown in Fig. 4, which presents intrinsic semiconductor-like absorption. The bandgap values were calculated according to the following empirical equation:

$$\alpha h\nu = A(h\nu - E_g)^{n/2}$$

where α, $h\nu$, A and E_g signify the absorption coefficient, photo energy, proportionality constant and bandgap, respectively. In the equation, n equals to 1 or 4, depending on whether the transition is direct or indirect. According to the following calculation $Nb_3O_7(OH)$ is an indirect gap semiconductor and the value of n for $Nb_3O_7(OH)$ was estimated to be 4. The energy of the bandgap is calculated by extrapolating a straight line to the abscissa axis. The inset of Fig. 4 shows the plot of $(\alpha h\nu)^{1/2}$ versus $h\nu$. The bandgaps of the products are estimated to be 2.85 eV.

Density functional theory (DFT) calculations were performed to evaluate the electronic structure of $Nb_3O_7(OH)$. Fig. 5 displays the contributions of each atom to the valence bands and conduction bands, and the partial and projected density of states (PDOS) of the $Nb_3O_7(OH)$ structure. The lowest unoccupied state lies at the Γ point, while the highest occupied state is at the Q point. This means that $Nb_3O_7(OH)$ is an indirect gap semiconductor. The excited electrons have to travel a certain k-space distance to be emitted to the valence band. This reduces the recombination opportunity of the excited electrons and holes, which benefits the hole–electron separation and charge transport. The calculated bandgap of $Nb_3O_7(OH)$ is 2.0 eV, which is smaller than the experimental value (2.85 eV), which results from not only the well-known shortcoming of the bandgap underestimation within the framework of standard DFT but also the crystal structure depending seriously on the temperature and experimental conditions. The wide valence band was also confirmed by the XPS valence band spectrum of $Nb_3O_7(OH)$ (Fig. S5, see ESI†). The valence-band maximum (VBM) is determined to be 2.82 eV.
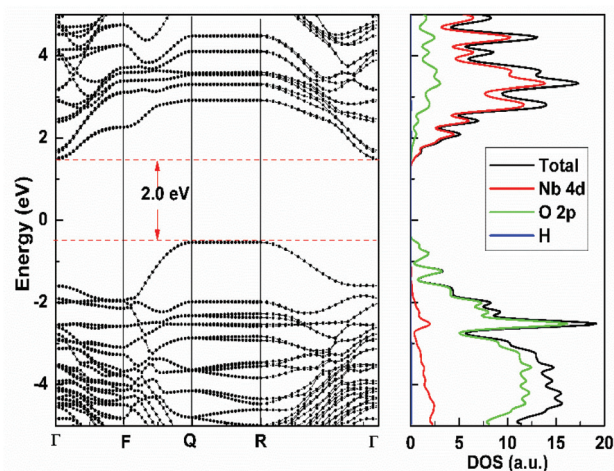
According to PDOS, the valence-band top as well as the conduction-band bottom is a hybridization of the O 2p and Nb 4d orbitals. The interaction between Nb and O atoms may also improve the generation and separation of the photoexcited electron–hole pairs, thus enhancing the photocatalytic activity of $Nb_3O_7(OH)$. The formation of impurity energy levels hybridized by O 2p states and Nb 4d states as the valence and conduction bands of the $Nb_3O_7(OH)$ structure leads to bandgap narrowing, which may result in the enhancement of photocatalytic absorption and activity under light irradiation. In addition, the existence of impurity energy levels that can be occupied by the photon-generated carrier can accelerate the separation efficiency of the electron and hole pairs.[32]

The photocatalytic activities of the as-prepared samples were evaluated by the degradation of RhB in water. Prior to irradiation under a 500 W Xe lamp, continuous incubation in the dark for 30 min led to the equilibrium adsorption of RhB molecules on the surfaces of the samples. The dependence of the RhB concentration (C) after irradiation against the concentration (C_0) at the equilibrium adsorption state versus the reaction time is plotted in Fig. 6. For comparison, the photocatalytic performances of the Nb_2O_5 replica and $Nb_3O_7(OH)$ with irregular shapes were also evaluated under the same conditions. RhB was completely photodegraded by the 3D $Nb_3O_7(OH)$ hierarchical nanostructures in 20 min, while about 45% and 60% RhB remained in the reaction as six-way sheaf-like Nb_2O_5 and irregular $Nb_3O_7(OH)$ powder, respectively. A control experiment in the absence of a photocatalyst under UV visible light irradiation revealed that RhB was not decomposed. This difference indicates that the obtained $Nb_3O_7(OH)$ plays a critical role for the efficient degradation of RhB under illumination. Another blank experiment in the presence of the as-synthesized $Nb_3O_7(OH)$ without irradiation demonstrated that the concentration of RhB remained unchanged as a function of time, namely, $Nb_3O_7(OH)$ acted as a photocatalyst to efficiently harvest photon energy to facilitate the decomposition reaction of RhB.

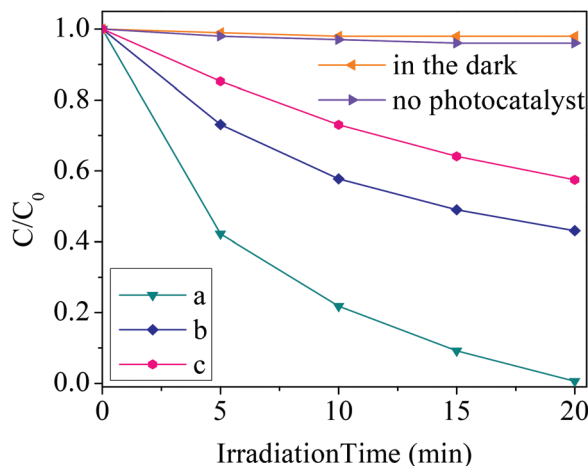**Fig. 6** Curves for the photocatalytic degradation of RhB by (a) 3D $Nb_3O_7(OH)$ hierarchical nanostructures, (b) Nb_2O_5 replica, and (c) irregular $Nb_3O_7(OH)$ powder.

Furthermore, after five recycles of the photodegradation of RhB (Fig. 7), the photocatalyst did not exhibit any significant loss of activity, confirming that $Nb_3O_7(OH)$ is not photocorroded during the photocatalytic oxidation of the pollutant molecules. The XRD and XPS results of the $Nb_3O_7(OH)$ after five cycles are shown in Fig. S6 and S7 (see ESI†). All the peaks of both XRD and XPS agree well with those of the fresh $Nb_3O_7(OH)$, which implies that $Nb_3O_7(OH)$ with hierarchical nanostructures exhibits good stability and could be used as a catalyst repeatedly (Fig. 7).

The photocatalytic activity is dominated by several factors such as the surface area, bandgap, oxidation potential of photogenerated holes, and the separation efficiency of photogenerated electrons and holes.[33–36] In the $Nb_3O_7(OH)$ system, the high photocatalytic activity of the 3D hierarchical nanostructures could be attributed to the following aspects. The obtained 3D $Nb_3O_7(OH)$ hierarchical nanostructures possess a high surface area, which provides the potential for stronger adsorption ability to RhB molecules and offers more active
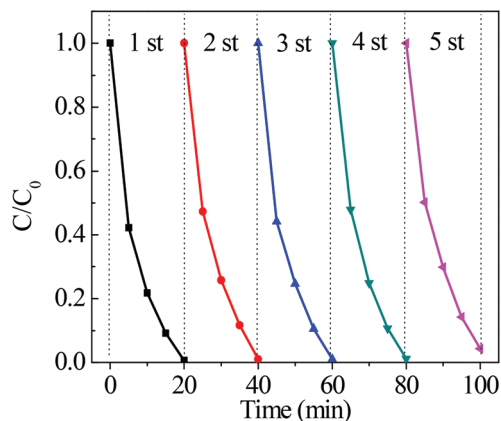
sites to adsorb water and hydroxyl groups for carrying out catalytic reactions.[37,38] The zeta potential of $Nb_3O_7(OH)$ hierarchical nanostructures dispersed in water (1 g L^{-1} in water) is 29.6 mV. However, RhB is slightly electronegative in an aqueous solution. Thus, the surface charge of $Nb_3O_7(OH)$ also contributes to the stronger adsorption capability of RhB molecules as a result of the interaction of the positive and negative charges. In addition, the existence of the H atom in $Nb_3O_7(OH)$ might also contribute to the high photocatalytic performance. The H atom in the $Nb_3O_7(OH)$ atomic structure bonds to one O atom in the (002) plane and interacts with another nearest O atom in the same plane *via* a hydrogen bond to form O–H·O.[24] The presence of the H atom induces more defects and hence results in the formation of new active sites. These new active sites could capture photogenerated electrons or holes and promote the separation efficiency of electron and hole pairs. Moreover, the surface functional group –OH in $Nb_3O_7(OH)$ could also be beneficial for the adsorption of hydrophilic groups and dye molecules. This would benefit the production of active ·OH radicals. These radicals can directly destroy the ring structure of the dye molecules and then convert them into CO_2 by either H atom abstraction, direct electron transfer, or insertion.

Conclusions

3D Hierarchical nanostructured $Nb_3O_7(OH)$ with a well-defined six-way sheaf-like morphology has been successfully synthesized as a novel photocatalyst for the first time, which is composed of numerous closely packed nanorods. The formation process of the hierarchical nanoarchitecture is attributed to the synergistic effects of Ostwald ripening and self-assembly processes. Furthermore, the 3D hierarchical $Nb_3O_7(OH)$ nanoarchitecture exhibits enhanced efficient photocatalytic performance for the decomposition of RhB and a favourable recycling capability. The high performance benefits from the unique microstructure, high surface area, and electronic structures. It is expected that the resulting 3D $Nb_3O_7(OH)$ nanostructures may offer great promise in other fields, such as preferential adsorption and water treatment.

Acknowledgements

Fig. 7 Cycling runs in the photocatalytic degradation of RhB in the presence of the as-formed 3D $Nb_3O_7(OH)$ nanostructures.

Notes and references

1 Z. L. Wang and J. Song, *Science*, 2006, **312**, 242–246.
2 S. C. Glotzer and M. J. Solomon, *Nat. Mater.*, 2007, **6**, 557–562.

3 C. Burda, X. Chen, R. Narayanan and M. A. El-Sayed, *Chem. Rev.*, 2005, **105**, 1025–1102.

4 X. L. Hu and J. C. Yu, *Adv. Funct. Mater.*, 2008, **18**, 880–887.

5 X. L. Hu, J. C. Yu, J. M. Gong, Q. Li and G. S. Li, *Adv. Mater.*, 2007, **19**, 2324–2329.

6 X. L. Hu, J. Gong, L. Zhang and J. C. Yu, *Adv. Mater.*, 2008, **20**, 4845–4850.

7 X. L. Hu, G. Li and J. C. Yu, *Langmuir*, 2009, **26**, 3031–3039.

8 J. H. Pan, G. Han, R. Zhou and X. S. Zhao, *Chem. Commun.*, 2011, **47**, 6942–6944.

9 L. Ye, W. Guo, Y. Yang, Y. Du and Y. Xie, *Chem. Mater.*, 2007, **19**, 6331–6337.

10 J. G. Yu, H. G. Yu, H. T. Guo, M. Li and S. Mann, *Small*, 2008, **4**, 87–91.

11 J. G. Yu, S. H. Wang, J. X. Low and W. Xiao, *Phys. Chem. Chem. Phys.*, 2013, **15**, 16883–16890.

12 K. Ariga, H. Ito, J. P. Hill and H. Tsukube, *Chem. Soc. Rev.*, 2012, **41**, 5800–5835.

13 X. F. Chen, X. C. Wang and X. Z. Fu, *Energy Environ. Sci.*, 2009, **2**, 872–877.

14 J. S. Zhang, J. H. Sun, K. Maeda, K. Domen, P. Liu, M. Antonietti, X. Z. Fu and X. C. Wang, *Energy Environ. Sci.*, 2011, **4**, 675–678.

15 M. Shang, W. Z. Wang, L. Zhang, S. M. Sun, L. Wang and L. Zhou, *J. Phys. Chem. C*, 2009, **113**, 14727–14731.

16 L. Zhang, W. Wang, L. Zhou and H. Xu, *Small*, 2007, **3**, 1618–1625.

17 J. Wu, F. Duan, Y. Zheng and Y. Xie, *J. Phys. Chem. C*, 2007, **111**, 12866–12871.

18 Y. Zhao, C. Eley, J. P. Hu, J. S. Foord, L. Ye, H. Y. He and S. C. Tsang, *Angew. Chem., Int. Ed.*, 2012, **51**, 3846–3849.

19 R. Jose, V. Thavasi and S. Ramakrishna, *J. Am. Ceram. Soc.*, 2009, **92**, 289–301.

20 A. L. Viet, M. V. Reddy, R. Jose, B. V. R. Chowdari and S. Ramakrishna, *J. Phys. Chem. C*, 2009, **114**, 664–671.

21 K. J. Range, M. Wildenauer and A. M. Heyns, *Angew. Chem., Int. Ed. Engl.*, 1988, **27**, 969–971.

22 F. Izumi and H. Kodama, *Z. Anorg. Allg. Chem.*, 1978, **441**, 196–204.

23 H. M. Zhang, Y. Wang, D. J. Yang, Y. B. Li, H. W. Liu, P. R. Liu, B. J. Wood and H. J. Zhao, *Adv. Mater.*, 2012, **24**, 1598–1603.

24 G. Kresse and J. Furthmuller, *Phys. Rev. B: Condens. Matter*, 1996, **54**, 11169–11185.

25 G. Kresse and D. Joubert, *Phys. Rev. B: Condens. Matter*, 1999, **59**, 1758–1774.

26 K. B. John, P. Perdew and M. Ernzerhof, *Phys. Rev. Lett.*, 1996, **77**, 3865–3868.

27 J. Heyd, G. E. Scuseria and M. Ernzerhof, *J. Chem. Phys.*, 2003, **118**, 8207–8215.

28 L. C. A. Oliveira, T. C. Ramalho, M. Gonçalves, F. Cereda, K. T. Carvalho, M. S. Nazzaro and K. Sapag, *Chem. Phys. Lett.*, 2007, **446**, 133–137.

29 A. Jasik, R. Wojcieszak, S. Monteverdi, M. Ziolek and M. M. Bettahar, *J. Mol. Catal. A: Chem.*, 2005, **242**, 81–90.

30 L. Zhou, W. Z. Wang, H. L. Xu, S. M. Sun and M. Shang, *Chem. – Eur. J.*, 2009, **15**, 1776–1782.

31 D. V. Bavykin, V. N. Parmon, A. A. Lapkin and F. C. Walsh, *J. Mater. Chem.*, 2004, **14**, 3370–3377.

32 Z. Wang, J. G. Hou, C. Yang, S. Q. Jiao, K. Huang and H. M. Zhu, *Phys. Chem. Chem. Phys.*, 2013, **15**, 3249–3255.

33 M. R. Hoffmann, S. T. Martin, W. Choi and D. W. Bahnemann, *Chem. Rev.*, 1995, **95**, 69–96.

34 S. B. Zhu, T. G. Xu, H. B. Fu, J. C. Zhao and Y. F. Zhu, *Environ. Sci. Technol.*, 2007, **41**, 6234–6239.

35 D. F. Hou, X. L. Hu, P. Hu, W. Zhang, M. F. Zhang and Y. H. Huang, *Nanoscale*, 2013, **5**, 9764–9772.

36 D. F. Hou, W. Luo, Y. H. Huang, J. C. Yu and X. L. Hu, *Nanoscale*, 2013, **5**, 2028–2035.

37 J. C. Yu, L. Z. Zhang, Z. Zheng and J. C. Zhao, *Chem. Mater.*, 2003, **15**, 2280–2286.

38 J. G. Yu, Q. Li, S. W. Liu and M. Jaroniec, *Chem. – Eur. J.*, 2013, **19**, 2433–2441.